

How the Layer Alignment in Two-Dimensional Nanoporous Covalent Organic Frameworks Impacts Its Electronic Properties

Kuber Singh Rawat, Sander Borgmans, Tom Braeckevelt, Christian V. Stevens, Pascal Van Der Voort, and Veronique Van Speybroeck*



Cite This: *ACS Appl. Nano Mater.* 2022, 5, 14377–14387



Read Online

ACCESS |



Metrics & More



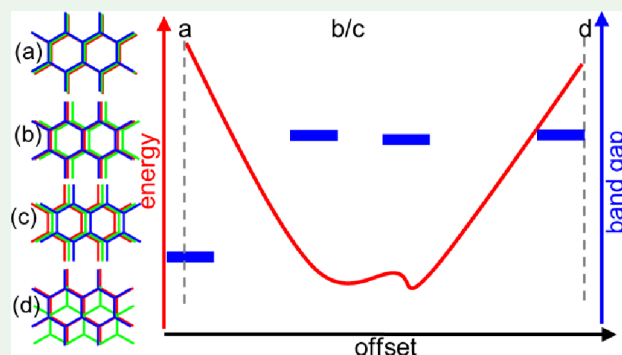
Article Recommendations



Supporting Information

ABSTRACT: Two-dimensional nanoporous covalent organic frameworks (2D COFs) have gathered significant interest due to their wide range of applications. Due to the lack of strong covalent interlayer interactions, their layers can be stacked in countless ways, each resulting in unique nanoscale characteristics impacting the structural, chemical, and electronic properties. To characterize and understand the layer stacking in 2D COFs and its effect on the structural and electronic properties, we carried out a detailed density functional theory investigation on four materials, CTF-1, COF-1, COF-5, and *Pc*-PBBA. This entailed an in-depth evaluation of the potential energy as a function of the interlayer distance and offset, the powder X-ray diffraction (PXRD) pattern, and the electronic properties. From the potential energy surfaces, the typical slipped AA-stacking configuration was confirmed as optimal for each of the 2D COFs, with a slight offset from a perfect alignment of the layers. The statically calculated PXRD patterns based on these optimized stacking configurations showed discrepancies when compared to experimental data. Instead, when properly accounting for dynamic fluctuations by calculating the average diffraction pattern over the course of a molecular dynamics simulation, a better agreement with the experiment is obtained. Different stacking configurations also profoundly affected the electronic band structure of COFs as the interlayer π - π interactions are significantly impacted by the layer offset. Evidently, with decreasing layer offsets, the π - π interactions increase due to the layer alignment, leading to a decrease in the band gap and an increase in interlayer charge mobility. Our study highlights the need for accurate modeling of the stacking configuration in 2D COFs as a small-scale deviation in the adjacent layer position can significantly affect the structural and electronic properties.

KEYWORDS: covalent organic frameworks, two-dimensional materials, mobility, band structure, stacking



1. INTRODUCTION

Covalent organic frameworks (COFs) are an emerging class of crystalline porous polymerized materials, consisting of organic building blocks with a huge structural diversity. Through the atomic-scale tunability of their organic building blocks, COFs can be applied in an ever-increasing range of applications, giving rise to numerous porous crystalline materials since their first introduction in 2005.^{1–7} Generally, these organic building blocks are made of lightweight and non-toxic elements, connected by strong covalent bonds, giving rise to a stable and robust material. These valuable nanoscale characteristics collectively make COFs a potential candidate for various crucial applications such as gas storage and separation,^{8–11} catalysis,^{12–15} energy storage,^{16–20} and optoelectronics.^{21,22} Depending on the geometry of the building blocks and their connectivity, COFs adopt either a nanoporous two-dimensional (2D) or three-dimensional (3D) framework. 2D COFs are layered structures, where individual layers are formed through covalent bonding of the building blocks, which are

stacked on top of each other. The relative layer position between these layers in the bulk structure is governed by the non-covalent interactions between them. In contrast, 3D COFs are completely bonded together by strong covalent bonds.

As a result of the weaker interactions between subsequent layers in 2D COFs, they possess a large intrinsic freedom in the relative positions of their layers. This freedom is typically divided into two orthogonal phase spaces: the layer offset (a vector in the plane of the layer) and the interlayer distance (ILD), where the former defines the alignment of the layers (Figure 1a,b).

Received: June 20, 2022

Accepted: August 24, 2022

Published: September 19, 2022



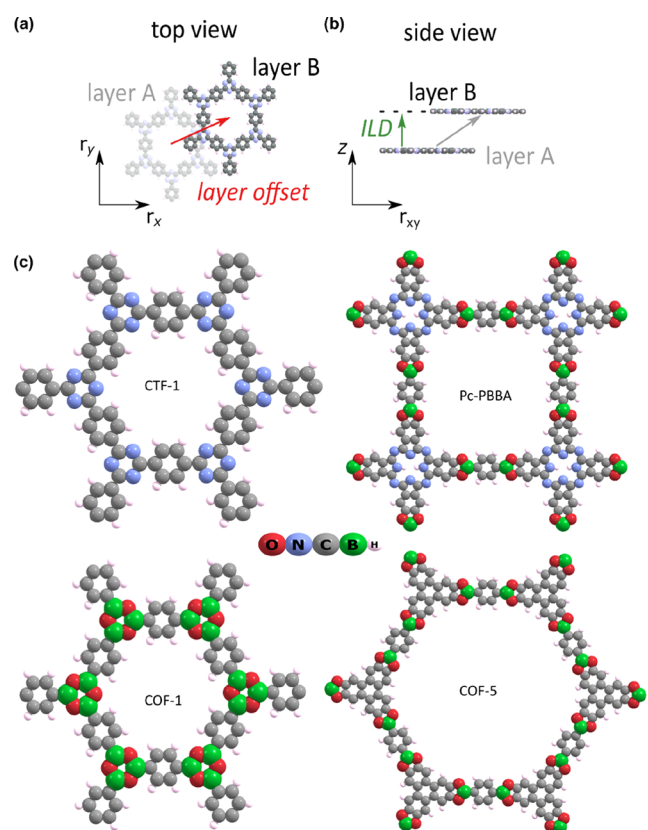


Figure 1. Schematic representation of (a) subsequent layer offset along the xy -plane and (b) interlayer distance along the z -direction. (c) Structures of the studied 2D COFs. The atom colors are elaborated in the figure.

The stacking configuration is typically labeled based on the aforementioned layer alignment (see Figure 2), such as the eclipsed stacking (AA), which is formed when there is a zero-offset vector between consecutive layers. However, in most cases, a small non-zero offset will be present, which is referred to as slipped AA-stacking.²³ This slipped AA-stacking is further classified into serrated AA-stacking, where the stacking between every other layer is eclipsed (AA'A...), and inclined AA-stacking, where the layer offset is always in the same direction (AA'A'...). Finally, the special case of serrated stacking where all vertices of one layer are exactly above the

pore centers of the consecutive layer will be labeled as staggered AB-stacking. These different types of stacking patterns strongly influence the physical and chemical nature of 2D COFs and derived material properties. Recently, different approaches have been explored to form a predesigned stacking pattern in 2D COFs. Bein and co-workers used propeller-shaped building blocks which drive consecutive COF sheets to lock into position, reducing the chances of unexpected layer offsets.²⁴ In another study, the interlayer steric hindrance was varied through a multivariate method to control the formation of AA- and AB-stacking in 2D COFs,²⁵ whereas Chen *et al.* introduced self-complementary π -electronic interactions between subsequent layers to control the stacking behavior.²⁶ Recently, Zhao and co-workers reported a different stacking configuration between the dried and the solvated material, when using an appropriate solvent. This change was driven by a solvation effect, which effectively increased the interlayer distance, decreasing the interlayer interactions and leading to changes in the equilibrium layer offset.²⁷ Moreover, particular synthetic routes have also been observed to favor a particular type of stacking in COF layers.^{28–30}

The aforementioned freedom in the phase space of the interlayer distance becomes evident when considering the typical broad diffraction peak at high diffraction angles in the powder X-ray diffraction (PXRD) patterns of 2D COFs.²³ This makes determining the exact interlayer distance difficult. Therefore, other than experimental studies, computational approaches contribute to investigate the stacking patterns and other properties of COFs.^{31–35} These studies show that a variation in the stacking configuration has a significant influence on the interlayer distance and the corresponding electronic properties. For COF-1, interlayer distances of 3.51 and 3.13 Å have been reported for eclipsed AA-stacking and AB-stacking, respectively,³¹ with the corresponding band gaps of 2.2 and 3.7 eV, respectively.³⁴ Clearly, it is crucial to investigate the stacking in 2D COFs as it affects the structural, mechanical, and electronic properties, which are essential in the prediction of their efficacy for their intended application.

In this current computational work, we have investigated the structural arrangement of four well known 2D COFs, CTF-1,² COF-1,¹ COF-5,¹ and Pc-PBBA³⁶ (Figure 1c). We have studied the interlayer stacking between two consecutive layers as a function of the two orthogonal phase spaces, the layer offset and the interlayer distance. We also compared the

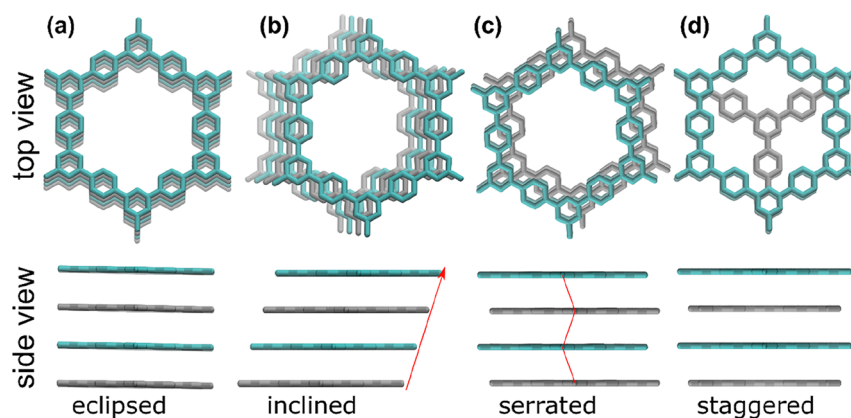


Figure 2. Different types of stacking in 2D COFs, namely, (a) eclipsed AA-stacking, (b) inclined AA-stacking, (c) serrated AA-stacking, and (d) staggered AB-stacking, viewed from either the top or the side.

density functional theory (DFT)-obtained interlayer distances with the interlayer distances obtained *via* the RPA + HF method. The RPA + HF method calculates the correlation energy *via* the random phase approximation (RPA) and the exchange energy *via* Hartree–Fock (HF) calculations using DFT orbitals obtained with the PBE XC functional as input. The RPA + HF method is in principle a fully *ab initio* method and is here used as the most accurate prediction for the interlayer distance.³⁷

To evaluate the effect of stacking on the electronic properties of COFs, their band structures were investigated in detail using the Heyd–Scuseria–Ernzerhof 06 (HSE06) hybrid functional.^{38,39} The PXRD patterns were also derived for each stacking configuration to investigate how they influence the diffraction pattern and to validate their geometry with respect to the experimental reference data.

2. COMPUTATIONAL DETAILS

The first-principles calculations were performed using a projector augmented wave (PAW)⁴⁰ basis set and the Perdew–Burke–Ernzerhof (PBE) functional⁴¹ with VASP.^{42–45} Grimme’s D3 dispersion corrections with Becke–Johnson damping were used in our calculations to account for the non-covalent interactions,^{46,47} whereas the hybrid functional (HSE06) was used when calculating band structures.^{38,39} The plane-wave basis cutoff energy was set to 600 eV, and all structures were optimized with an electronic energy convergence threshold of 10^{-6} eV and an ionic relaxation threshold of 10^{-5} eV. The PAW PBE potentials were used with the $1s^1$, $2s^2 2p^1$, $2s^2 2p^2$, $2s^2 2p^3$, and $2s^2 2p^4$ valence electron configurations for the H, B, C, N, and O atoms, respectively. A one-layer unit cell was considered while investigating the eclipsed and inclined AA-stacking, whereas a two-layer unit cell was considered for the serrated AA-stacking and staggered AB-stacking. For CTF-1 and COF-1, a $2 \times 2 \times 4$ Γ -centered grid was used to sample the Brillouin zone for both the one- and two-layer unit cells. We also tested the $2 \times 2 \times 8$ Γ -centered grids for the one-layer unit cell for CTF-1. However, we found that the energy difference between these k -point grids was only 0.01 kJ/mol. COF-5 and *Pc*-PBBA were studied using $1 \times 1 \times 5$ and $1 \times 1 \times 7$ Γ -centered grids, respectively, for the one-layer cell, and a $1 \times 1 \times 3$ Γ -centered grid was used for the two-layer unit cell.

To calculate the potential energy surface (PES) as a function of the layer offset vector, described by its x - and y -components, a minimal grid size was used, leveraging the symmetry of the unit cell. For the honeycomb lattice COFs (COF-1, COF-5, and CTF-1), this corresponded to 1/12th of a hexagon (a right triangle with an angle of 30°). For inclined AA-stacking in CTF-1 and COF-1, the triangle legs were $3 \text{ \AA} \times 1.6 \text{ \AA}$, totaling 78 structures when using a 0.2 \AA step size. For COF-5, the triangle legs were $5 \text{ \AA} \times 2.8 \text{ \AA}$ to account for the larger unit cell, totaling 201 structures. For *Pc*-PBBA, which has a square lattice, 1/8th of a square (a right triangle with an angle of 45°) was considered with dimensions of $5 \text{ \AA} \times 4.8 \text{ \AA}$, totaling 326 structures. For serrated AA-stacking in CTF-1, COF-1, and COF-5, the triangle legs were $3 \text{ \AA} \times 1.6 \text{ \AA}$, totaling 78 structures, whereas for *Pc*-PBBA, dimensions of $3 \text{ \AA} \times 2.8 \text{ \AA}$ were used with 121 structures. The corresponding stacking energy (E_s) of the COF layers was also calculated using eq 1

$$E_s = \frac{E_{nl}}{n} - E_m \quad (1)$$

where n is the number of layers in the unit cell, E_{nl} is the total energy of n number of layers stacking in a COF, and E_m is the total energy of a monolayer of a COF. We also benchmarked the performance of the different exchange–correlation (XC) functionals and the dispersion method. The detailed computational information is given in the Supporting Information (Text S1).

To generate the PXRD patterns, molecular dynamics (MD) calculations were performed with the CP2K software package.^{48,49} The PBE-D3(BJ) functional was used in combination with the Gaussian and Plane Wave (GPW)^{50,51} basis set approach. The TZVP-GTH basis set and GTH pseudopotentials were used⁵² with a cutoff energy of 800 Ry and a relative cutoff of 40 Ry for all atoms. A super cell of six layers was considered for all the MD calculations where the Γ -point was sufficient for such a large system. For example, in the MD simulation of CTF-1, a $2 \times 2 \times 6$ supercell was considered. As such, the first Brillouin zone of the supercell is $2 \times 2 \times 6$ times smaller with respect to the initial unit cell, effectively reproducing the $2 \times 2 \times 6$ k -point grid density of the small unit cell in VASP with only the Γ -point in CP2K. The MD simulations employed a velocity Verlet integration scheme, with a timestep of 0.5 fs, amounting to a total simulation time of at least 10 ps for each simulation. To mimic realistic operating conditions, the *NPT* ensemble was used, allowing the unit cell shape and size to vary freely. The pressure was controlled at 1 atm, monitored using a Martyna–Tobias–Klein (MTK) barostat using a time constant of 1 ps.⁵³ The temperature (300 K) was controlled using a Nosé–Hoover chain thermostat with five beads and a time constant of 100 fs.^{54–56}

3. RESULTS AND DISCUSSION

We have studied four types of possible stackings in 2D COFs (Figure 2). In the case of inclined AA-stacking (Figure 2b) and serrated AA-stacking (Figure 2c), we first investigated the influence of a varying layer offset, while keeping the interlayer distance fixed. Subsequently, the optimal value of the interlayer distance was determined for each favorable stacking configuration. A full PES analysis would require varying both the interlayer distance and the layer offset at the same time (a 3D grid), resulting in an 11-fold increase of the number of simulations (equal to the number of grid spacings in the z -direction). Consequently, for computational feasibility, the phase spaces were separated. In particular, for eclipsed AA-stacking (Figure 2a) and staggered AB-stacking (Figure 2d), only the interlayer distances were varied as these stacking configurations have a fixed layer offset. Finally, after the most optimal layer offset and interlayer distance were determined for each stacking configuration, the most favorable stacking was considered by comparing the relative and stacking energies. Furthermore, the most favorable structures were used for each stacking to determine their static PXRD patterns and electronic properties.

3.1. Layer Offset. To investigate the most favorable stacking in CTF-1, at a constant interlayer distance, we examined the inclined and serrated AA-stacking modes. The zero-shift layered/eclipsed CTF-1 was taken as an initial structure for our study. For inclined stacking (Figure 2b), each consecutive layer is displaced, and for the serrated mode (Figure 2c), the odd- and even-numbered layers are eclipsed separately, with a fixed layer offset between consecutive even- and odd-numbered layers, as illustrated in Figure 2. To

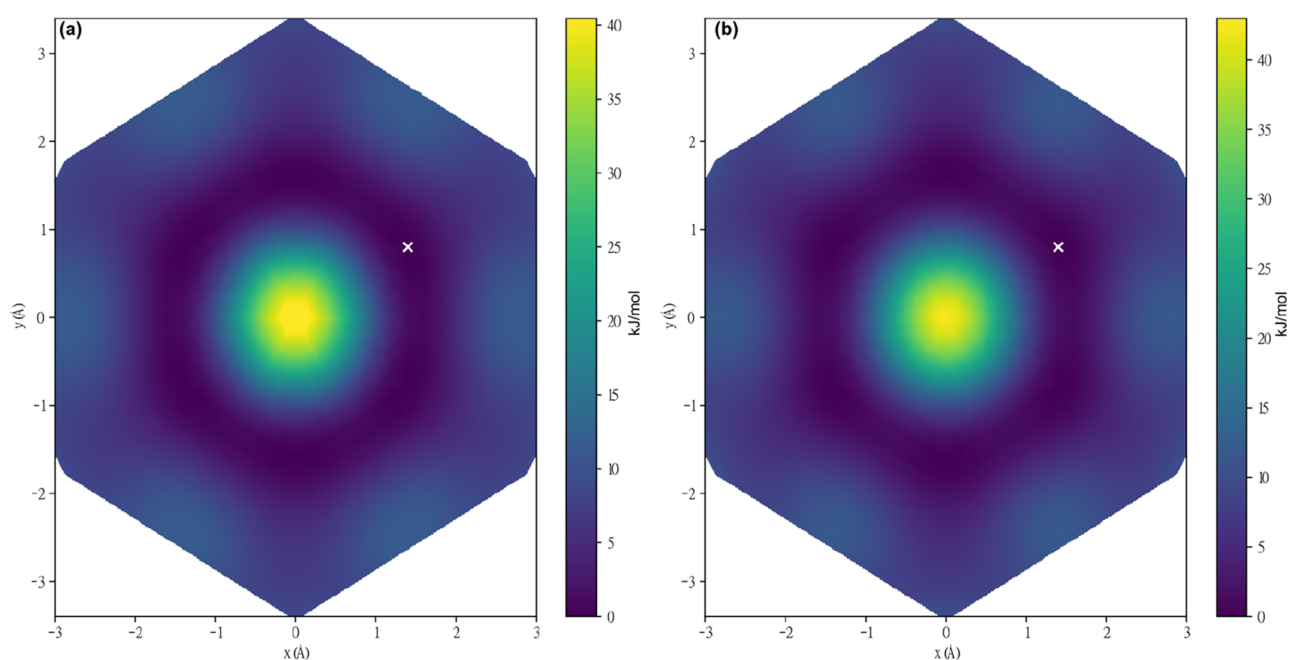


Figure 3. Contour plots visualizing the PES as a function of the layer offset vector for (a) inclined AA-stacking (at a fixed interlayer distance of 3.38 Å) and (b) serrated AA-stacking (at a fixed interlayer distance of 3.36 Å) in CTF-1 using PBE-D3(BJ). The white cross shows the most stable configuration. The unit cell consists of one layer and two layers for inclined and serrated stacking, respectively. The energy of the most stable configuration was set to zero for each stacking configuration separately.

understand how the shift between the layers affects the total energy of the COF, the layer shift was varied with a step size of 0.2 Å at a fixed interlayer distance (3.38 Å). The calculated PES (Figure 3) suggests that as the layers move away from each other, the structure becomes more energetically favorable compared to the initial structure until a quasi-directionally independent layer offset distance, after which the energy increases again. The most stable configurations were again relaxed to calculate the global minima, which are obtained at 1.74 and 1.67 Å away from the center for the inclined and serrated stackings, respectively. These stacking patterns reveal that the eclipsed AA-stacking (Figure 2a) is not an energetically favorable configuration for CTF-1 and instead prefers an inclined or serrated stacking configuration.

3.2. Interlayer Distance. After obtaining the energetically most favorable stacking in CTF-1, the optimal interlayer distance was explored for inclined and serrated AA-stacking configurations *via* single-point calculations. For this, five steps with a step size of 0.01 Å were considered in the $-z$ and $+z$ directions near the global minima. In order to get an optimal correspondence with respect to the experimental value (3.40 Å),² we considered various XC functionals and dispersion methods, as listed in Table 1, and tested for inclined AA-stacking. The accuracy of the used XC functional and dispersion method was benchmarked by comparing the obtained interlayer distances for different XC functionals with fully *ab initio* RPA + HF calculations and with experiments. The RPA + HF results are used as the most accurate prediction of the interlayer distance at 0 K. The calculated RPA + HF interlayer distance is 0.09 Å lower when compared to the experiment, which is in line with the general observation that the interlayer distance increases with temperature. An equal or lower interlayer distance is also observed for all other functionals except the vdW-DF2 XC functional.

Table 1. Calculated Interlayer Distances of CTF-1 for Inclined AA-Stacking with Different Levels of Theory

functional	interlayer distance (Å)
experimental value	3.40
PBE + D2	3.24
PBE + D3(BJ)	3.36
PBE + D3(BJ) ^{ATM}	3.34
PBE + TS	3.31
PBE + MBD	3.38
PBE + MBD/FI	3.37
B3LYP + D3(BJ)	3.28
B3LYP + D3(BJ) ^{ATM}	3.28
HSE06 + D3(BJ)	3.39
HSE06 + D3(BJ) ^{ATM}	3.40
SCAN	3.39
SCAN + rVV10	3.28
vdW-DF2	3.44
M06-L	3.29
RPA + HF	3.31

Moreover, aside from the vdW-DF2 and PBE + D2 XC functionals, all interlayer distances are between 3.28 and 3.40 Å, which corresponds closely to the 3.31–3.40 Å interval between the RPA + HF and experimental results. Therefore, almost all considered XC functionals are suitable to calculate the structural properties of the 2D COFs investigated in this work. In view of computational feasibility and accuracy, the PBE-D3(BJ) functional was chosen for all COFs as using PBE-D3(BJ) results in an interlayer distance of 3.36 Å for inclined AA-stacking, which is between the experimental (3.40 Å) and RPA + HF (3.31 Å) values. Using PBE-D3(BJ), the calculated interlayer distances suggest that the optimal distance is 3.36 and 3.38 Å for inclined stacking and serrated stacking, respectively (see Figure 4). Moreover, eclipsed AA and staggered AB were also considered for the interlayer distance

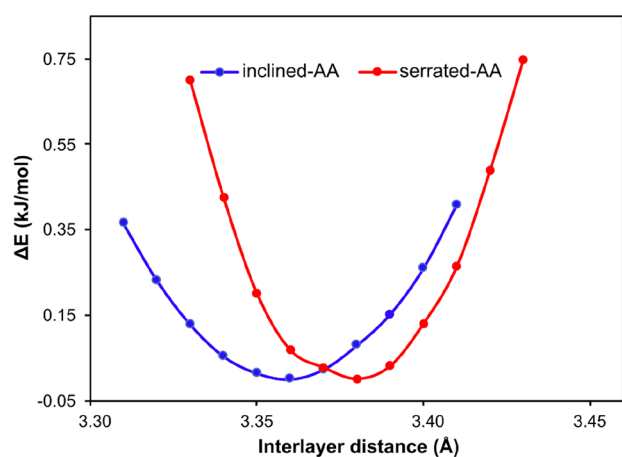


Figure 4. Variation of the energy as a function of the interlayer distance for inclined AA-stacking (blue) and serrated AA-stacking (red) of CTF-1. The energy of the most stable interlayer distance for each stacking is set to zero.

assessment (Table 2) and were found to have energetically stable structures for the interlayer distances of 3.68 and 3.17 Å, respectively.

Table 2. Calculated Offset and Interlayer Distance (ILD) between Neighboring Layers [Using PBE-(D3-BJ)] and the Band Gap (B. G.) of CTF-1 (Using HSE06)^a

stacking	offset (Å)	ILD (Å)	B.G. (eV)	R.E. (kJ/mol)	E_s (kJ/mol)
eclipsed AA	0.0	3.68	2.73	24.08	-87.5
inclined AA	1.74	3.36	3.18	0.0	-111.58
serrated AA	1.67	3.38	3.26	0.10	-111.48
staggered AB	8.09	3.17	3.22	19.67	-91.91
experimental		3.40 ²	2.95 ⁵⁷		

^aThe relative energy (R.E.) per layer is calculated with respect to the inclined AA-stacked structure and stacking energy per monolayer (E_s). All the energies were calculated using PBE-D3(BJ).

The interlayer distance in eclipsed CTF-1 is 0.28 Å higher than the experimental value (3.40 Å), whereas for the staggered AB configuration, it is 0.23 Å lower. The effective interlayer distance follows from the interplay between dispersive and electrostatic interactions.³⁴ The dispersive interactions stabilize the layers at a certain distance but become very repulsive below this equilibrium distance (Pauli repulsion), whereas the electrostatic interactions depend on the specific chemical nature of the interacting moieties. In the case of perfectly aligned layers, that is, AA stacking, the dispersive interactions are maximized, while the electrostatic interactions are maximally repulsive as identical charges are minimally separated. In contrast, for staggered AB-stacking (Figure 5), the misalignment of the layers minimizes the dispersion interactions, significantly lowering the repulsive dispersive interactions as there are fewer atoms in close proximity, while oppositely charged atoms in subsequent layers are now minimally separated, leading to a lower optimal interlayer distance. In CTF-1, the oppositely charged atoms in AB-stacking correspond to an inversion symmetry between the triazine rings in subsequent layers.

Further, we compared the energetic stability of these different stacking configurations based on the total energy (Table 2) and calculated the stacking energy (E_s). We found

that the inclined AA is the most stable stacking for CTF-1 and is very closely followed by serrated AA with a 0.10 kJ/mol/layer energy difference. This almost negligible energy difference likely results in the material exhibiting a mixture of both stacking configurations simultaneously when considering a large number of layers. The eclipsed AA-stacking and staggered AB-stacking configurations are 24.08 and 19.67 kJ/mol/layer less stable than the inclined stacking, respectively. These results reveal that neighboring layers do not desire to be stacked in an eclipsed mode and prefer to slip over each other to minimize the repulsion in line with the aforementioned interplay of dispersive and electrostatic interactions.

The stability of the most favorable stacking modes (inclined and serrated) was also confirmed *via* our MD simulation. The MD simulations were performed for CTF-1 starting from the eclipsed AA-stacked configuration as an initial structure. Through tracking of the layer alignment, it is clear that during the MD simulation, the neighboring layers immediately displace from the initial perfect alignment (Figure S1) and achieve average offset values close to the statically calculated offset values (inclined AA: 1.74 Å and serrated AA: 1.67 Å). This confirms the stability of the most favorable stacking modes (inclined and serrated) which were identified through both static calculations (scanning method) and MD simulation. A movie is given in the Supporting Information (Movie S1) to visualize how the layers displace from the initial perfect eclipsed stacking during the simulation.

3.3. Powder X-Ray Diffraction. PXRD measurements provide invaluable insights into the geometry of periodic crystal structures and are typically used to characterize the atomic representation of new materials. Through judicious comparison of the experimental reference pattern with the calculated diffraction pattern of possible structural models, the parameters of the structural models can be refined to obtain the material structure that maximally reproduces the experiment. Similarly, PXRD patterns were calculated for various stacking configurations of CTF-1 to validate which configuration corresponds best to the experimentally synthesized material. However, instead of optimizing the structural parameters, *ab initio* calculations were performed to obtain physically sound structural models. This gave rise to a collection of energetically favored stacking configurations at 0 K. However, as elaborated in our previous work,⁵⁸ a static approach to calculate the diffraction patterns introduces large discrepancies with the experiment due to an artificially decreased symmetry in the structures. As such, a dynamic approach was also considered, which accounted for the inherent temporal character of experimental measurements by considering an average PXRD pattern over the course of an MD simulation subjected to a finite pressure and temperature.

This is demonstrated in Figure 6, where the static (i–iv) and dynamic (v) results are compared to the experimental reference pattern, with a notably better correspondence for the dynamic average. Although the AA-stacked configuration provides a good correspondence with the experiment, it is thermodynamically not likely to occur, as evidenced from our potential energy scans. This is in contrast with the physically sound slipped stacking structures, which contain excess diffraction peaks due to their reduced symmetry. The seemingly resulting contradiction is resolved by the dynamic approach, which reproduces both the symmetry and the physical soundness of the structure by accounting for multiple stacking configurations simultaneously with an average AA-

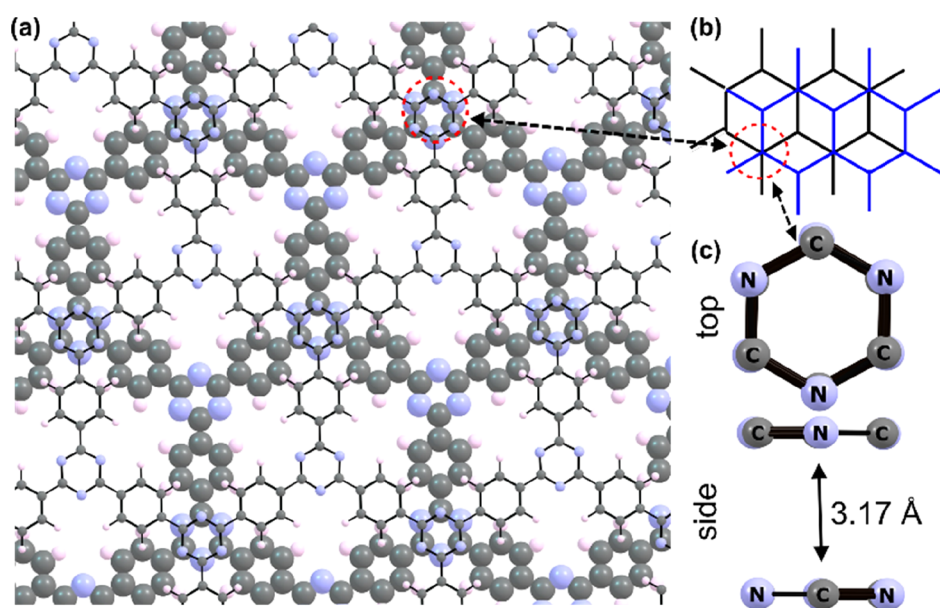


Figure 5. Staggered AB-stacking in CTF-1, as illustrated in (a) and schematically in (b), results in alternating vertices on top of each other (triazine moieties), indicated by the dotted circles. (c) Top and side view of triazine rings where the top and bottom layer cross each other. The atom sizes of the top layer in (a) were reduced for clarity.

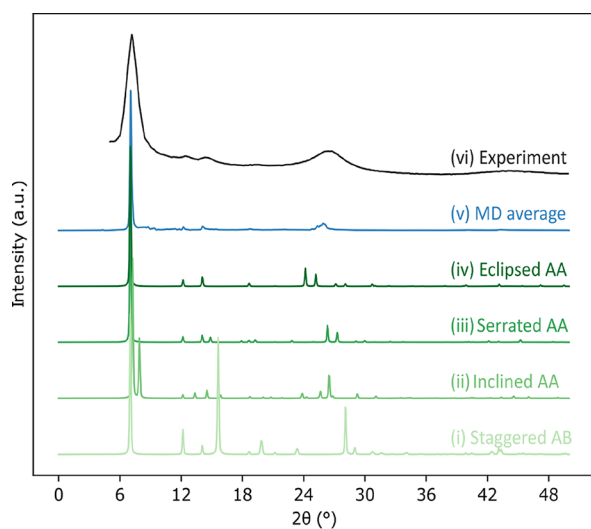


Figure 6. Simulated diffraction patterns for different CTF-1 stacking configurations, (i) staggered AB-stacking, (ii) inclined AA-stacking, (iii) serrated AA-stacking, and (iv) eclipsed AA-stacking. (v) Diffraction pattern obtained by averaging snapshots of the MD trajectory compared to the (vi) experimental reference pattern from ref 2. As the MD trajectory allows for the interlayer distance to fluctuate, a broad peak is obtained at $2\theta = 25^\circ$ in correspondence with the experiment.

stacking. Six independent layers accommodated this in our MD simulation (Figure S1), which shows that the layer slipping is omnipresent in the global structure, and a perfect eclipsed AA-stacking never occurs (aside from the initial configuration). This is driven by a minimal energy difference between different slipped stacking configurations (0.10 kJ/mol/layer), resulting in an optimal correspondence with the experimental diffraction pattern. Therefore, these simulated PXRD patterns suggest that the dynamic approach offers more accurate predictions for the experimental structures and validates the possibility of slipped stackings (inclined and/or serrated).

3.4. Electronic Properties. To determine how the electronic characteristics of CTF-1 are influenced by the stacking modes, band structures and the density of states (DOS) were calculated (Figure 7). The band gap was first calculated using the PBE functional. The calculated band gaps (Table S1) are 1.94, 2.35, 2.43, and 2.30 eV for eclipsed, inclined, serrated, and staggered stacking, respectively. This already shows a non-negligible dependence of the band gap on the specific stacking configuration. In general, the PBE functional underestimates the band gap; therefore, the hybrid HES06 functional was employed to calculate the band gaps with better accuracy. All four stacking configurations of CTF-1 are indirect band semiconductors, with eclipsed stacking (Figure 7a) possessing the smallest band gap of 2.73 eV (between Γ and A points). The band gap increases to 3.18, 3.26, and 3.22 eV for inclined, serrated, and staggered AB-stacking, respectively. These trends reveal the strength of the π - π interactions between the layers. More π - π interactions between the layers decrease the band gap, which is clearly found in the case of eclipsed stacking. In eclipsed AA-stacking, the orbitals are perfectly aligned with the orbitals of neighboring layers, which increases the π - π interactions between them and leads to a lower band gap (Figure 7a). For the other stackings, the offset reduces the π - π interactions between the layers (Figure 7). The interlayer interactions in the bulk 2D material also influence the band gaps of the material compared to the monolayer.^{59,60} To examine this effect in CTF-1, the band structure and the DOS of the monolayer were also investigated (Figure S2). A band gap of 3.63 eV was calculated for the CTF-1 monolayer, which is 0.9 eV more compared to the eclipsed stacked mode. This decrease in the band gap from monolayer to eclipsed stacking is due to increased π - π interactions between the adjacent layers of the stacked system. The decrease in the band gap is small for all other stacking configurations compared to the eclipsed stacking as the π - π interactions between the layers are reduced. The VB, originating from the k -points in the xy -plane, is flat, revealing the monolayer's lack of π -conjugation.

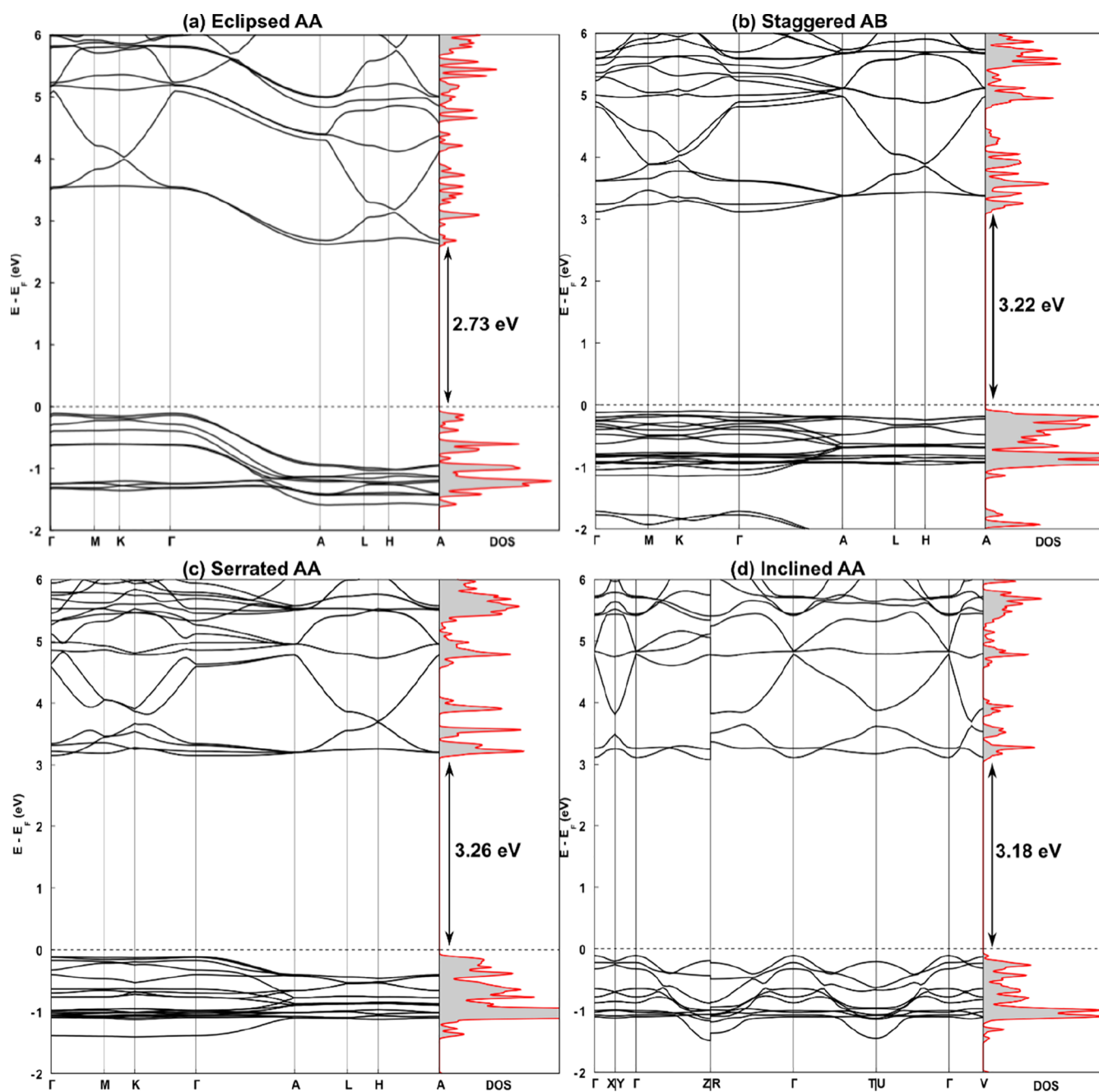


Figure 7. Band structure and density of states of (a) eclipsed AA-, (b) staggered AB-, (c) serrated AA-, and (d) inclined AA-stacking for CTF-1 using the HSE06 functional. The Fermi level is shifted to zero and specified by the gray dashed line.

Similar flat bands were found for the xy -plane in reciprocal space for all four stacking configurations. This is shown in Figure 7a–c by the Γ (0,0,0) to M (0.5,0,0), M to K (0.33,0.33,0), K to Γ , A (0,0,0.5) to L (0.5,0,0.5), L to H (0.33,0.33,0.5), and H to A paths of the band structure. This indicates a decreased π -conjugation, leading to a low charge carrier mobility in the xy -plane of the COF. To improve the electron delocalization *via* π -conjugation along the xy -plane, experimentalists take advantage of sp^2 carbon-conjugated frameworks.^{61,62} These sp^2 carbon-conjugated-based COFs demonstrated extended π -conjugation along the 2D lattice, promoting the layer alignment through π - π interactions. In Figure 7d, a different high-symmetry path in reciprocal space was investigated as the inclined AA-stacking configuration has

another space group (triclinic) compared to the other stacking configurations. Moreover, we cannot deduce the charge mobility within the layer from the band structure depicted in Figure 7d because the out-of-plane unit cell vector is not orthogonal to the in-plane unit cell vector for inclined AA-stacking.

The situation changes in the z -direction (Γ -A), more specifically for eclipsed stacking, where, due to interlayer orbital interactions, a strong band dispersion occurs in the vertical direction of the layers. This results in better electronic mobility between the layers through perpendicular π - π interactions between the layers. This agrees well with previous experimental findings that charge flows perpendicular to the 2D COF layers.^{63–65} The calculated effective masses (Table 3)

Table 3. Calculated Effective Mass of the Electron (m_e^*) and Hole (m_h^*)^a

stacking	m_h^*	m_e^*
eclipsed AA	-1.111 ($\Gamma \rightarrow A$)	1.355 ($A \rightarrow \Gamma$)
serrated AA	-1.661 ($\Gamma \rightarrow A$)	
inclined AA	-1.410 ($\Gamma \rightarrow Z$)	2.645 ($Z \rightarrow \Gamma$)
staggered AB	-2.879 ($K \rightarrow \Gamma$)	3.353 ($\Gamma \rightarrow A$)

^aAll values are expressed in terms of the free-electron mass m_0 .

of $-1.11m_0$ and $1.36m_0$ of the hole and electron along the z -direction also indicate the high carrier mobility in eclipsed AA-stacking with respect to $-2.88m_0$ and $3.35m_0$ in staggered AB-stacking, respectively. For a deeper understanding of orbital alignment and contribution, band decomposed charge densities of the valence band maximum (VBM), and conduction band minimum (CBM) were analyzed (Figures S3, S4), along with the partial density of states (pDOS) and partial band structures (Figure S5). The results reveal that the orbitals of adjacent layers are perfectly aligned on top of each other in eclipsed stacking, which leads to strong π - π orbital interactions (Figure S3). The perfect orbital alignment is shifted for serrated AA- and inclined AA-stacking configurations, leading to reduced π - π interactions between the layers, with a maximal orbital shift for staggered AB. The pDOS and partial band structure also show that the p-orbitals of carbon and nitrogen contribute to the VB and CB, which increase the possibility of orbital interactions. Here, each neighboring layer contributes an equal density to the DOS (Figure S6). This suggests that the layer offset should be minimized for charge-transfer-related applications, with an eclipsed AA-stacked structure as the ideal material.

Finally, two stacking configurations with a minimal symmetry were constructed (Figure S7a,b), with a fixed interlayer distance and layer offset distance but a random offset direction, to understand the influence of the third layer on the electronic properties. Starting from the optimal AA-serrated stacking configuration, the c -vector was adapted to obtain unique stacking configurations such that two symmetrically inequivalent stacking directions were present in the periodic

structure. This resulted in structures with both inclined and serrated features. The calculated band structures (Figure S7c) show that the orientation of the third layer with respect to the first is mainly uncorrelated and has minor effects on the electronic properties due to screening effects. The remaining mismatch can be attributed to the difference between the k -path and offset directions. Generally, in these 2D COFs, the layers will be randomly stacked with a fixed offset length with respect to the neighboring layers.²³ This is also evident from our MD simulations and validates the approach to only consider the nearest neighboring layers. As such, by scanning over all two-layer configurations as in Figure 3, we include all relevant configurations.

3.5. Other 2D COFs. Similar to CTF-1, other 2D COFs (COF-1, COF-5, and *Pc*-PBBA) were also explored in detail (Figure S8). The corresponding results of the optimal layer offset, interlayer distance, band gaps, and relative energy differences for the studied stacking configurations are reported in Table 4. The calculated offsets are within a range of 1.60–1.88 Å for inclined and serrated stacking. Previously, Zojer and co-workers reported an offset of 1.75 Å for serrated stacking in COF-1, which agrees well with our calculated offset of 1.74 Å for the serrated COF-1.³⁴ Heine and co-workers also reported an offset of 1.4 Å for COF-1 and COF-5.³² We observe that similar to CTF-1, all these 2D COFs also prefer the inclined and serrated AA-stacking configurations with higher interaction energies when compared to eclipsed AA- and staggered AB-stacking configurations. For COF-1, the inclined stacking is more favorable over serrated stacking with an energy difference of 1.43 kJ/mol, whereas COF-5 stabilizes in serrated stacking with a 1.0 kJ/mol energy difference when compared to an inclined stacking; thus, both stackings are possible. This is in good agreement with previous computational reports, which indicated that serrated stacking is desirable for COF-1 and COF-5. However, they did not include the inclined stacking in their study.³⁴ In the case of *Pc*-PBBA, both inclined and serrated stacking configurations are equally favorable. Moreover, the interlayer distance also displays a similar trend when compared to CTF-1, where the optimal interlayer distance for serrated and inclined stacking is very close to the experimental

Table 4. Calculated Offset and Interlayer Distance (ILD) of Neighboring Layers [Using PBE-D3(BJ)] and Band Gap (B.G.) of COF-1, COF-5, and *Pc*-PBBA (Using HSE06)^a

COFs	stacking	offset (Å)	ILD (Å)	B.G. (eV)	R.E. (kJ/mol)	E_s (kJ/mol)
COF-1	eclipsed	0.0	3.74, (3.62), ³⁴ (3.51), ³¹ (3.38) ³³	3.37 (2.2), ³⁴ (3.3) ³¹	38.65	-68.60
	inclined AA	1.88	3.35	3.94	0.0	-107.25
	serrated AA	1.74, (1.75) ³⁴	3.40, (3.36) ³⁴	3.98 (3.7) ³⁴	1.43	-105.82
	staggered AB	8.76	3.08, (3.13) ³¹	4.04, (3.6) ³¹	16.68	-90.57
	experimental		3.33 ¹			
COF-5	eclipsed AA	0.0	3.72, (3.59), ³⁴ (3.49), ³³ (3.47) ³¹	2.30, (2.06), ³⁴ (2.4) ³¹	60.73	-177.38
	inclined AA	1.66	3.40	2.84	1.0	-237.12
	serrated AA	1.61	3.41, (3.39) ³⁴	2.76, (2.70) ³⁴	0.0	-238.12
	staggered AB	17.54	3.40, (3.26) ³³	3.06, (2.8) ³¹	149.97	-88.14
	experimental		3.46 ¹			
<i>Pc</i> -PBBA	eclipsed AA	0.0	3.68	0.93	63.18	-162.13
	inclined AA	1.83	3.33	1.56	0.0	-225.31
	serrated AA	1.62	3.39	1.54	0.0	-255.31
	staggered AB	16.20	3.60	1.72	164.11	-61.20
	experimental		3.34 ³⁶			

^aThe relative energy (R.E.) per layer is calculated with respect to the most favorable stacked configuration and stacking energy per monolayer (E_s). Previously reported computational values are given in parentheses. All the energies were calculated using PBE-D3(BJ).

value. Notably, the eclipsed AA-stacking shows a ~ 0.30 Å higher interlayer distance when compared to the inclined and serrated stackings for all the calculated 2D COFs.

We found that for COF-5 and *Pc*-PBBA, the interlayer distance for the staggered AB-stacking is also high (close to inclined and serrated AA-stacking for COF-5 and close to eclipsed AA-stacking for *Pc*-PBBA), which contrasts with CTF-1 and COF-1. The reason for this different trend for AB-stacking is that the AB-stacking does not result in stabilizing electrostatic interactions between opposite charges such that only the misalignment effect occurs, which is similar for all slipped stacking configurations (Figure S9). Overall, we find that all the investigated 2D COFs favor serrated and inclined stacking configurations as the layers are more stable when they are displaced from each other. Consecutive layers are typically offset by 1.60–1.88 Å, which optimally reduces the Pauli repulsion between them.

After locating the energetically desired stacking and interlayer distance, the electronic properties and PXRD patterns of other 2D COFs were also considered. The PXRD patterns calculated using a dynamic approach agree well with the experimental patterns (Figure S10). The calculated band gaps using the PBE functional are given in Table S1. Likewise, the electronic properties using the HSE06 functional display similar trends in the bands and band gaps as for CTF-1 (Figures S11–S13). The band gap increases from eclipsed AA-stacking to other stacking configurations due to the lack of π – π interactions between the layers in other stacking modes. The highest band gap, for each COF, was found for the monolayer (Table S1 and Figure S14). Similar to CTF-1, the considered 2D COFs are characterized by flat bands, originating from *k*-points between the high-symmetry points in the reciprocal *xy*-plane, corresponding to a lack of charge mobility within the layers. However, *Pc*-PBBA also shows flat bands in the perpendicular direction for other stacking configurations because of the reduced π – π orbital interactions. We also compared our calculated band gaps with previously reported theoretical studies. For COF-1, the band gaps of 2.2 and 3.7 eV have been reported for eclipsed and serrated stacking, respectively.³⁴ A band gap of 3.3 eV was also stated in another study on COF-1 for eclipsed stacking.³¹ Other previously reported values are given in Table 4. We observe that the band gaps of all stacking modes for COF-5 are comparable with the previous values and have a minimal spread of ~ 0.30 eV.^{31,34} This is also true for the stacking modes COF-1, except for the eclipsed AA-stacking configuration. The calculated band gap is 3.37 eV, which is 1.17 eV more compared to the previously reported value (2.2 eV) for eclipsed AA COF-1.³⁴ The calculated effective mass (Table S2) suggests that the highest charge mobility can be found along the *z*-direction for eclipsed AA-stacking in both COF-1 and COF-5. In contrast, for *Pc*-PBBA, the maximal charge mobility is found along the *xy*-plane.

4. CONCLUSIONS

We have carried out a detailed investigation of the stacking behavior of four very well-known nanoporous 2D COFs, CTF-1, COF-1, COF-5, and *Pc*-PBBA, with an in-depth evaluation of energetics, stackings, interlayer distance, electronic properties, and PXRD patterns. One of the primary findings, based on the energetics, is that the slipped AA-stacking, either inclined or serrated, is more favorable over eclipsed AA- and staggered AB-stackings for all four 2D COFs. The minor energy

difference between inclined and serrated stackings suggests that both can be present in the same system to maintain the offset with neighboring layers. This was validated by the PXRD patterns of the 2D COFs simulated using the more realistic dynamic approach *via* MD trajectories, which accurately match the experimental PXRD patterns. Moreover, the interlayer distance for inclined and serrated stackings agrees well with experimental values, further supporting the slipped stacking arrangements. We observe that the nature of the electronic band structure is strongly affected by the stacking modes in COF nanostructures. For all 2D COFs, the eclipsed stacking configurations are associated with the lowest band gaps as a consequence of stronger interlayer π – π interactions. The band structures of all stacked modes are flat in the *xy*-plane, which explains the low in-plane electron mobility of 2D COFs. However, the interlayer π – π interaction results in more dispersed bands and improves the electron mobility in the *z*-direction, which is maximum for eclipsed AA-stacking configurations. Evidently, tuning the structure to promote eclipsed stacking would be an essential step toward electronic applications. Overall, our work provides a basis for understanding the structural and electronic complexity in 2D COFs and the role of stacking. We believe that such a detailed description of the structural dependency of electronic properties will be valuable to both computational and experimental researchers to target the desired applications with directed modifications of COFs.

■ ASSOCIATED CONTENT

SI Supporting Information

The Supporting Information is available free of charge at <https://pubs.acs.org/doi/10.1021/acsnm.2c02647>.

Computational details; layer offset as a function of MD simulation time; band gaps using the PBE functional; band structure and DOS for the CTF-1 monolayer; band-decomposed charge density; partial band structure and pDOS for CTF-1; cell variations in serrated AA-stacking and the related band structure and DOS; contour plots; PXRD patterns; and band structures, DOS, and effective mass for COF-1, COF-5, and *Pc*-PBBA (PDF)

Final coordinates of atoms in all the relevant stacking configurations and initial structures for MD calculations (ZIP)

MD trajectory for CTF-1 from both top and side views, illustrating the layer alignment variations (MP4)

■ AUTHOR INFORMATION

Corresponding Author

Veronique Van Speybroeck – Center for Molecular Modeling (CMM), Ghent University, Zwijnaarde 9052, Belgium;
orcid.org/0000-0003-2206-178X;
Email: veronique.vanspeybroeck@ugent.be

Authors

Kuber Singh Rawat – Center for Molecular Modeling (CMM), Ghent University, Zwijnaarde 9052, Belgium;
orcid.org/0000-0002-7308-4204

Sander Borgmans – Center for Molecular Modeling (CMM), Ghent University, Zwijnaarde 9052, Belgium

Tom Braeckvelt – Center for Molecular Modeling (CMM), Ghent University, Zwijnaarde 9052, Belgium

Christian V. Stevens – SynBioC Research Group, Department of Green Chemistry and Technology, Ghent University, Ghent 9000, Belgium; orcid.org/0000-0003-4393-5327

Pascal Van Der Voort – COMOC-Center for Ordered Materials, Organometallics and Catalysis, Department of Chemistry, Ghent University, Ghent 9000, Belgium; orcid.org/0000-0002-1248-479X

Complete contact information is available at:
<https://pubs.acs.org/10.1021/acsnm.2c02647>

Notes

The authors declare no competing financial interest.

ACKNOWLEDGMENTS

This work was supported by the Research Board of Ghent University (BOF) through a Concerted Research Action (GOA010-17). T.B. acknowledges the Fund for Scientific Research–Flanders (FWO) for a strategic basic (SB) research fellowship (grant no. 15C1319N). The computational resources (Stevin Supercomputer Infrastructure) and services used in this work were provided by the VSC (Flemish Supercomputer Center), funded by Ghent University, FWO, and the Flemish Government – department EWI.

REFERENCES

- (1) Côté, A. P.; Benin, A. I.; Ockwig, N. W.; O’Keeffe, M.; Matzger, A. J.; Yaghi, O. M. Porous, Crystalline, Covalent Organic Frameworks. *Science* **2005**, *310*, 1166–1170.
- (2) Kuhn, P.; Antonietti, M.; Thomas, A. Porous, Covalent Triazine-Based Frameworks Prepared by Ionothermal Synthesis. *Angew. Chem., Int. Ed.* **2008**, *47*, 3450–3453.
- (3) El-Kaderi, H. M.; Hunt, J. R.; Mendoza-Cortés, J. L.; Côté, A. P.; Taylor, R. E.; O’Keeffe, M.; Yaghi, O. M. Designed Synthesis of 3D Covalent Organic Frameworks. *Science* **2007**, *316*, 268–272.
- (4) Uribe-Romo, F. J.; Hunt, J. R.; Furukawa, H.; Klöck, C.; O’Keeffe, M.; Yaghi, O. M. A Crystalline Imine-Linked 3-D Porous Covalent Organic Framework. *J. Am. Chem. Soc.* **2009**, *131*, 4570–4571.
- (5) Côté, A. P.; El-Kaderi, H. M.; Furukawa, H.; Hunt, J. R.; Yaghi, O. M. Reticular Synthesis of Microporous and Mesoporous 2D Covalent Organic Frameworks. *J. Am. Chem. Soc.* **2007**, *129*, 12914–12915.
- (6) Han, S. S.; Furukawa, H.; Yaghi, O. M.; Goddard, W. A. Covalent Organic Frameworks as Exceptional Hydrogen Storage Materials. *J. Am. Chem. Soc.* **2008**, *130*, 11580–11581.
- (7) Liu, Y.-Y.; Li, X.-C.; Wang, S.; Cheng, T.; Yang, H.; Liu, C.; Gong, Y.; Lai, W.-Y.; Huang, W. Self-Templated Synthesis of Uniform Hollow Spheres Based on Highly Conjugated Three-Dimensional Covalent Organic Frameworks. *Nat. Commun.* **2020**, *11*, 5561.
- (8) Kang, Z.; Peng, Y.; Qian, Y.; Yuan, D.; Addicoat, M. A.; Heine, T.; Hu, Z.; Tee, L.; Guo, Z.; Zhao, D. Mixed Matrix Membranes (MMMs) Comprising Exfoliated 2D Covalent Organic Frameworks (COFs) for Efficient CO₂ Separation. *Chem. Mater.* **2016**, *28*, 1277–1285.
- (9) Baldwin, L. A.; Crowe, J. W.; Pyles, D. A.; McGrier, P. L. Metalation of a Mesoporous Three-Dimensional Covalent Organic Framework. *J. Am. Chem. Soc.* **2016**, *138*, 15134–15137.
- (10) Wang, G.; Leus, K.; Jena, H. S.; Krishnaraj, C.; Zhao, S.; Depauw, H.; Tahir, N.; Liu, Y.-Y.; Van Der Voort, P. A Fluorine-Containing Hydrophobic Covalent Triazine Framework with Excellent Selective CO₂ Capture Performance. *J. Mater. Chem. A* **2018**, *6*, 6370–6375.
- (11) Fan, H.; Mundstock, A.; Feldhoff, A.; Knebel, A.; Gu, J.; Meng, H.; Caro, J. Covalent Organic Framework–Covalent Organic Framework Bilayer Membranes for Highly Selective Gas Separation. *J. Am. Chem. Soc.* **2018**, *140*, 10094–10098.
- (12) Fang, Q.; Gu, S.; Zheng, J.; Zhuang, Z.; Qiu, S.; Yan, Y. 3D Microporous Base-Functionalized Covalent Organic Frameworks for Size-Selective Catalysis. *Angew. Chem., Int. Ed.* **2014**, *53*, 2878–2882.
- (13) Krishnaraj, C.; Sekhar Jena, H.; Bourda, L.; Laemont, A.; Pachfule, P.; Roeser, J.; Chandran, C. V.; Borgmans, S.; Rogge, S. M. J.; Leus, K.; Stevens, C. V.; Martens, J. A.; Van Speybroeck, V.; Breynaert, E.; Thomas, A.; Van Der Voort, P. Strongly Reducing (Diaryl-amino)Benzene-Based Covalent Organic Framework for Metal-Free Visible Light Photocatalytic H₂O₂ Generation. *J. Am. Chem. Soc.* **2020**, *142*, 20107–20116.
- (14) Chen, H.; Liu, W.; Laemont, A.; Krishnaraj, C.; Feng, X.; Rohman, F.; Meledina, M.; Zhang, Q.; Van Deun, R.; Leus, K.; Van Der Voort, P. A Visible-Light-Harvesting Covalent Organic Framework Bearing Single Nickel Sites as a Highly Efficient Sulfur–Carbon Cross-Coupling Dual Catalyst. *Angew. Chem., Int. Ed.* **2021**, *60*, 10820–10827.
- (15) Zou, Y.; Abednatanzi, S.; Gohari Derakhshandeh, P.; Mazzanti, S.; Schüßlbauer, C. M.; Cruz, D.; Van Der Voort, P.; Shi, J.-W.; Antonietti, M.; Guldi, D. M.; Savateev, A. Red Edge Effect and Chromoselective Photocatalysis with Amorphous Covalent Triazine-Based Frameworks. *Nat. Commun.* **2022**, *13*, 2171.
- (16) Lei, Z.; Yang, Q.; Xu, Y.; Guo, S.; Sun, W.; Liu, H.; Lv, L.-P.; Zhang, Y.; Wang, Y. Boosting Lithium Storage in Covalent Organic Framework via Activation of 14-Electron Redox Chemistry. *Nat. Commun.* **2018**, *9*, 576.
- (17) Talapaneni, S. N.; Hwang, T. H.; Je, S. H.; Buyukcakir, O.; Choi, J. W.; Coskun, A. Elemental-Sulfur-Mediated Facile Synthesis of a Covalent Triazine Framework for High-Performance Lithium-Sulfur Batteries. *Angew. Chem.* **2016**, *128*, 3158–3163.
- (18) Wang, S.; Wang, Q.; Shao, P.; Han, Y.; Gao, X.; Ma, L.; Yuan, S.; Ma, X.; Zhou, J.; Feng, X.; Wang, B. Exfoliation of Covalent Organic Frameworks into Few-Layer Redox-Active Nanosheets as Cathode Materials for Lithium-Ion Batteries. *J. Am. Chem. Soc.* **2017**, *139*, 4258–4261.
- (19) Wang, S.; Li, X.; Cheng, T.; Liu, Y.; Li, Q.; Bai, M.; Liu, X.; Geng, H.; Lai, W.-Y.; Huang, W. Highly Conjugated Three-Dimensional Covalent Organic Frameworks with Enhanced Li-Ion Conductivity as Solid-State Electrolytes for High-Performance Lithium Metal Batteries. *J. Mater. Chem. A* **2022**, *10*, 8761–8771.
- (20) Liu, X.; Liu, C.-F.; Xu, S.; Cheng, T.; Wang, S.; Lai, W.-Y.; Huang, W. Porous Organic Polymers for High-Performance Supercapacitors. *Chem. Soc. Rev.* **2022**, *51*, 3181–3225.
- (21) Yadav, V. K.; Mir, S. H.; Mishra, V.; Gopakumar, T. G.; Singh, J. K. A Simple Molecular Design for Tunable Two-Dimensional Imine Covalent Organic Frameworks for Optoelectronic Applications. *Phys. Chem. Chem. Phys.* **2020**, *22*, 21360–21368.
- (22) Song, Y.; Sun, Q.; Aguila, B.; Ma, S. Opportunities of Covalent Organic Frameworks for Advanced Applications. *Adv. Sci.* **2019**, *6*, 1801410.
- (23) Pütz, A. M.; Terban, M. W.; Bette, S.; Haase, F.; Dinnebier, R. E.; Lotsch, B. V. Total Scattering Reveals the Hidden Stacking Disorder in a 2D Covalent Organic Framework. *Chem. Sci.* **2020**, *11*, 12647–12654.
- (24) Ascherl, L.; Sick, T.; Margraf, J. T.; Lapidus, S. H.; Calik, M.; Hettstedt, C.; Karaghiosoff, K.; Döblinger, M.; Clark, T.; Chapman, K. W.; Auras, F.; Bein, T. Molecular Docking Sites Designed for the Generation of Highly Crystalline Covalent Organic Frameworks. *Nat. Chem.* **2016**, *8*, 310–316.
- (25) Wu, X.; Han, X.; Liu, Y.; Liu, Y.; Cui, Y. Control Interlayer Stacking and Chemical Stability of Two-Dimensional Covalent Organic Frameworks via Steric Tuning. *J. Am. Chem. Soc.* **2018**, *140*, 16124–16133.
- (26) Chen, X.; Addicoat, M.; Irlé, S.; Nagai, A.; Jiang, D. Control of Crystallinity and Porosity of Covalent Organic Frameworks by Managing Interlayer Interactions Based on Self-Complementary π -Electronic Force. *J. Am. Chem. Soc.* **2013**, *135*, 546–549.
- (27) Kang, C.; Zhang, Z.; Wee, V.; Usadi, A. K.; Calabro, D. C.; Baugh, L. S.; Wang, S.; Wang, Y.; Zhao, D. Interlayer Shifting in Two-

Dimensional Covalent Organic Frameworks. *J. Am. Chem. Soc.* **2020**, *142*, 12995–13002.

(28) Li, H.; Shao, P.; Chen, S.; Li, G.; Feng, X.; Chen, X.; Zhang, H.-J.; Lin, J.; Jiang, Y.-B. Supramolecular Alternating Donor–Acceptor Assembly toward Intercalated Covalent Organic Frameworks. *J. Am. Chem. Soc.* **2020**, *142*, 3712–3717.

(29) Haase, F.; Gottschling, K.; Stegbauer, L.; Germann, L. S.; Gutzler, R.; Duppel, V.; Vyas, V. S.; Kern, K.; Dinnebier, R. E.; Lotsch, B. V. Tuning the Stacking Behaviour of a 2D Covalent Organic Framework through Non-Covalent Interactions. *Mater. Chem. Front.* **2017**, *1*, 1354–1361.

(30) Yang, Z.; Chen, H.; Wang, S.; Guo, W.; Wang, T.; Suo, X.; Jiang, D.; Zhu, X.; Popovs, I.; Dai, S. Transformation Strategy for Highly Crystalline Covalent Triazine Frameworks: From Staggered AB to Eclipsed AA Stacking. *J. Am. Chem. Soc.* **2020**, *142*, 6856–6860.

(31) Lukose, B.; Kuc, A.; Frenzel, J.; Heine, T. On the Reticular Construction Concept of Covalent Organic Frameworks. *Beilstein J. Nanotechnol.* **2010**, *1*, 60–70.

(32) Lukose, B.; Kuc, A.; Heine, T. The Structure of Layered Covalent–Organic Frameworks. *Chem.—Eur J.* **2011**, *17*, 2388–2392.

(33) Zhou, W.; Wu, H.; Yildirim, T. Structural Stability and Elastic Properties of Prototypical Covalent Organic Frameworks. *Chem. Phys. Lett.* **2010**, *499*, 103–107.

(34) Winkler, C.; Kamencek, T.; Zojer, E. Understanding the Origin of Serrated Stacking Motifs in Planar Two-Dimensional Covalent Organic Frameworks. *Nanoscale* **2021**, *13*, 9339–9353.

(35) Zhang, Y.; Polozij, M.; Heine, T. Statistical Representation of Stacking Disorder in Layered Covalent Organic Frameworks. *Chem. Mater.* **2022**, *34*, 2376–2381.

(36) Spittler, E. L.; Dichtel, W. R. Lewis Acid-Catalysed Formation of Two-Dimensional Phthalocyanine Covalent Organic Frameworks. *Nat. Chem.* **2010**, *2*, 672–677.

(37) Chen, G. P.; Voora, V. K.; Agee, M. M.; Balasubramani, S. G.; Furche, F. Random-Phase Approximation Methods. *Annu. Rev. Phys. Chem.* **2017**, *68*, 421–445.

(38) Heyd, J.; Scuseria, G. E.; Ernzerhof, M. Hybrid Functionals Based on a Screened Coulomb Potential. *J. Chem. Phys.* **2003**, *118*, 8207–8215.

(39) Krukau, A. V.; Vydrov, O. A.; Izmaylov, A. F.; Scuseria, G. E. Influence of the Exchange Screening Parameter on the Performance of Screened Hybrid Functionals. *J. Chem. Phys.* **2006**, *125*, 224106.

(40) Kresse, G.; Joubert, D. From Ultrasoft Pseudopotentials to the Projector Augmented-Wave Method. *Phys. Rev. B: Condens. Matter Mater. Phys.* **1999**, *59*, 1758–1775.

(41) Perdew, J. P.; Burke, K.; Ernzerhof, M. Generalized Gradient Approximation Made Simple. *Phys. Rev. Lett.* **1996**, *77*, 3865–3868.

(42) Kresse, G.; Hafner, J. Ab Initio Molecular Dynamics for Liquid Metals. *Phys. Rev. B: Condens. Matter Mater. Phys.* **1993**, *47*, 558–561.

(43) Kresse, G.; Hafner, J. Ab Initio Molecular-Dynamics Simulation of the Liquid-Metal–Amorphous-Semiconductor Transition in Germanium. *Phys. Rev. B: Condens. Matter Mater. Phys.* **1994**, *49*, 14251–14269.

(44) Kresse, G.; Furthmüller, J. Efficiency of Ab-Initio Total Energy Calculations for Metals and Semiconductors Using a Plane-Wave Basis Set. *Comput. Mater. Sci.* **1996**, *6*, 15–50.

(45) Kresse, G.; Furthmüller, J. Efficient Iterative Schemes for Ab Initio Total-Energy Calculations Using a Plane-Wave Basis Set. *Phys. Rev. B: Condens. Matter Mater. Phys.* **1996**, *54*, 11169–11186.

(46) Grimme, S.; Ehrlich, S.; Goerigk, L. Effect of the Damping Function in Dispersion Corrected Density Functional Theory. *J. Comput. Chem.* **2011**, *32*, 1456–1465.

(47) Grimme, S.; Antony, J.; Ehrlich, S.; Krieg, H. A Consistent and Accurate Ab Initio Parametrization of Density Functional Dispersion Correction (DFT-D) for the 94 Elements H–Pu. *J. Chem. Phys.* **2010**, *132*, 154104.

(48) Hutter, J.; Iannuzzi, M.; Schiffmann, F.; VandeVondele, J. cp2k: atomistic simulations of condensed matter systems. *Wiley Interdiscip. Rev. Comput. Mol. Sci.* **2014**, *4*, 15–25.

(49) VandeVondele, J.; Krack, M.; Mohamed, F.; Parrinello, M.; Chassaing, T.; Hutter, J. Quickstep: Fast and Accurate Density Functional Calculations Using a Mixed Gaussian and Plane Waves Approach. *Comput. Phys. Commun.* **2005**, *167*, 103–128.

(50) Lippert, G.; Hutter, J.; Parrinello, M. A Hybrid Gaussian and Plane Wave Density Functional Scheme. *Mol. Phys.* **1997**, *92*, 477–487.

(51) Lippert, G.; Hutter, J.; Parrinello, M. The Gaussian and Augmented-Plane-Wave Density Functional Method for Ab Initio Molecular Dynamics Simulations. *Theor. Chem. Acc.* **1999**, *103*, 124–140.

(52) Goedecker, S.; Teter, M.; Hutter, J. Separable Dual-Space Gaussian Pseudopotentials. *Phys. Rev. B: Condens. Matter Mater. Phys.* **1996**, *54*, 1703–1710.

(53) Martyna, G. J.; Tobias, D. J.; Klein, M. L. Constant Pressure Molecular Dynamics Algorithms. *J. Chem. Phys.* **1994**, *101*, 4177–4189.

(54) Nosé, S. A Unified Formulation of the Constant Temperature Molecular Dynamics Methods. *J. Chem. Phys.* **1984**, *81*, 511–519.

(55) Nosé, S. A Molecular Dynamics Method for Simulations in the Canonical Ensemble. *Mol. Phys.* **1984**, *52*, 255–268.

(56) Hoover, W. G. Canonical Dynamics: Equilibrium Phase-Space Distributions. *Phys. Rev. A* **1985**, *31*, 1695–1697.

(57) Meier, C. B.; Sprick, R. S.; Monti, A.; Guiglian, P.; Lee, J.-S. M.; Zwijnenburg, M. A.; Cooper, A. I. Structure-Property Relationships for Covalent Triazine-Based Frameworks: The Effect of Spacer Length on Photocatalytic Hydrogen Evolution from Water. *Polymer* **2017**, *126*, 283–290.

(58) Borgmans, S.; Rogge, S. M. J.; De Vos, J. S.; Stevens, C. V.; Van Der Voort, P.; Van Speybroeck, V. Quantifying the Likelihood of Structural Models through a Dynamically Enhanced Powder X-Ray Diffraction Protocol. *Angew. Chem., Int. Ed.* **2021**, *60*, 8913–8922.

(59) Gutzler, R. Band-Structure Engineering in Conjugated 2D Polymers. *Phys. Chem. Chem. Phys.* **2016**, *18*, 29092–29100.

(60) Jiang, X.; Wang, P.; Zhao, J. 2D Covalent Triazine Framework: A New Class of Organic Photocatalyst for Water Splitting. *J. Mater. Chem. A* **2015**, *3*, 7750–7758.

(61) Jin, E.; Asada, M.; Xu, Q.; Dalapati, S.; Addicoat, M. A.; Brady, M. A.; Xu, H.; Nakamura, T.; Heine, T.; Chen, Q.; Jiang, D. Two-Dimensional Sp² Carbon–Conjugated Covalent Organic Frameworks. *Science* **2017**, *357*, 673–676.

(62) Chen, R.; Shi, J.-L.; Ma, Y.; Lin, G.; Lang, X.; Wang, C. Designed Synthesis of a 2D Porphyrin-Based Sp² Carbon–Conjugated Covalent Organic Framework for Heterogeneous Photocatalysis. *Angew. Chem., Int. Ed.* **2019**, *58*, 6430–6434.

(63) Jin, S.; Ding, X.; Feng, X.; Supur, M.; Furukawa, K.; Takahashi, S.; Addicoat, M.; El-Khouly, M. E.; Nakamura, T.; Irle, S.; Fukuzumi, S.; Nagai, A.; Jiang, D. Charge Dynamics in A Donor–Acceptor Covalent Organic Framework with Periodically Ordered Bicontinuous Heterojunctions. *Angew. Chem., Int. Ed.* **2013**, *52*, 2017–2021.

(64) Feng, X.; Chen, L.; Honsho, Y.; Saengsawang, O.; Liu, L.; Wang, L.; Saeki, A.; Irle, S.; Seki, S.; Dong, Y.; Jiang, D. An Ambipolar Conducting Covalent Organic Framework with Self-Sorted and Periodic Electron Donor–Acceptor Ordering. *Adv. Mater.* **2012**, *24*, 3026–3031.

(65) Feng, X.; Liu, L.; Honsho, Y.; Saeki, A.; Seki, S.; Irle, S.; Dong, Y.; Nagai, A.; Jiang, D. High-Rate Charge-Carrier Transport in Porphyrin Covalent Organic Frameworks: Switching from Hole to Electron to Ambipolar Conduction. *Angew. Chem., Int. Ed.* **2012**, *51*, 2618–2622.